International Journal of Mechanical Sciences 267 (2024) 109018

Contents lists available at ScienceDirect

International Journal of Mechanical Sciences

journal homepage: www.elsevier.com/locate/ijmecsci

Anomalous fracture behavior of soft layered materials

Yijie Cai, Shaoxing Qu, Zheng Jia *

State Key Laboratory of Fluid Power and Mechatronic Systems, Key Laboratory of Soft Machines and Smart Devices of Zhejiang Province, Center for X-Mechanics, Department of Engineering Mechanics, Zhejiang University, Hangzhou 310027, China

ARTICLE INFO

Keywords:
Soft materials
Fracture
Finite elastic deformation
Heterogeneous layered structure
Interfacial delamination

ABSTRACT

Soft layered material systems are ubiquitous in nature and engineering – from natural biological tissues to engineered devices. However, from the mechanics perspective, why soft layered materials are favored by natural selection and engineering design remains largely unexplored. Here we study the fracture mechanics of heterogeneous soft layered materials. We develop a theoretical framework for analyzing the co-evolving channel cracking and interfacial delamination in soft film/substrate systems, which is then applied on investigating the fracture of bilayer hydrogels – a representative soft layered material. Through both experiment investigation, theoretical analysis and numerical modeling, we find that the heterogeneous soft layered materials exhibit anomalous size-independent fracture behaviors with fracture strains independent of the flaw size and overall structural dimensions, in stark contrast to ordinary homogeneous materials whose stretch at break reduces undesirably with increasing flaw size and structural dimensions. The size-independent fracture behavior leads to notable toughening of soft layered materials. The findings hold for a broad range of hyperelastic soft materials, from biological materials to hydrogels and elastomers, opening potentially new avenues for the development of fracture-resistant soft materials, and motivating new investigations of the development and applications of heterogeneous soft materials.

1. Introduction

Derived from nature, soft materials including elastomers and hydrogels have played a pivotal role in enabling a wide range of modern technologies, becoming one of the most focused areas in recent years. Elastomers possess distinctive characteristics such as stability in diverse environments, mechanical robustness, and ease of micro-/nano-scale fabrication (e.g., through methods like soft lithography). Meanwhile, hydrogels also exhibit unique properties including high water content, permeability to a wide range of chemical and biological molecules, as well as biocompatibility and/or biodegradability [1–4]. Capitalizing on these advantages, elastomers and hydrogels have thus gained significant attention in the biomedical field, finding applications as wound dressing [5,6], drug delivery [7,8], tissue repair [9,10] and cell stimulators [11], Moreover, their application extends beyond the medical field, finding utility in non-medical areas serving as ionic loudspeakers [12], artificial muscles [13–15], artificial skins [16], ionotronic luminescent devices [17,18], soft robots [19,20] and all-solid-state supercapacitors [21]. In the above scenarios, soft material systems are often subjected to large and repeated deformation, such that cracks may initiate and propagate in the material, which causes the deterioration of structural performance and function of soft material systems. Notably, many soft material systems – from natural to synthetic – are layered for their electronic properties, chemical stabilities, and structural performances, with applications ranging over a broad spectrum of areas. Examples include natural human epidermis and epithelial cell sheets [22] in the human body (Fig. 1a), and artificial systems such as ionic skins [17,23–26] and hydrogel actuators [12,27,28] for soft ionotronics (Fig. 1b) as well as tissue adhesives [29–31] and tendon repairs [32,33] for biomedical applications (Fig. 1c). These material systems consisting of soft materials layered together are often referred to as soft layered materials.

Given the prevalence of soft layered materials in nature and engineering practice, a largely unexplored question emerges: what are the mechanical advantages of soft layered materials that render them favored by natural selection and engineering design? In this aspect, although it is recognized that forming layered structures can enhance the ability of soft materials to withstand substantial mechanical loads without failure, there is still a lack of comprehensive analysis and a clear understanding of the underlying mechanisms. In contrast to the rapid advancements in function design, the investigation of failure mechanics

* Corresponding author.
E-mail address: zheng.jia@zju.edu.cn (Z. Jia).

https://doi.org/10.1016/j.ijmecsci.2024.109018
Received 5 November 2023; Received in revised form 27 December 2023; Accepted 4 January 2024
Available online 5 January 2024

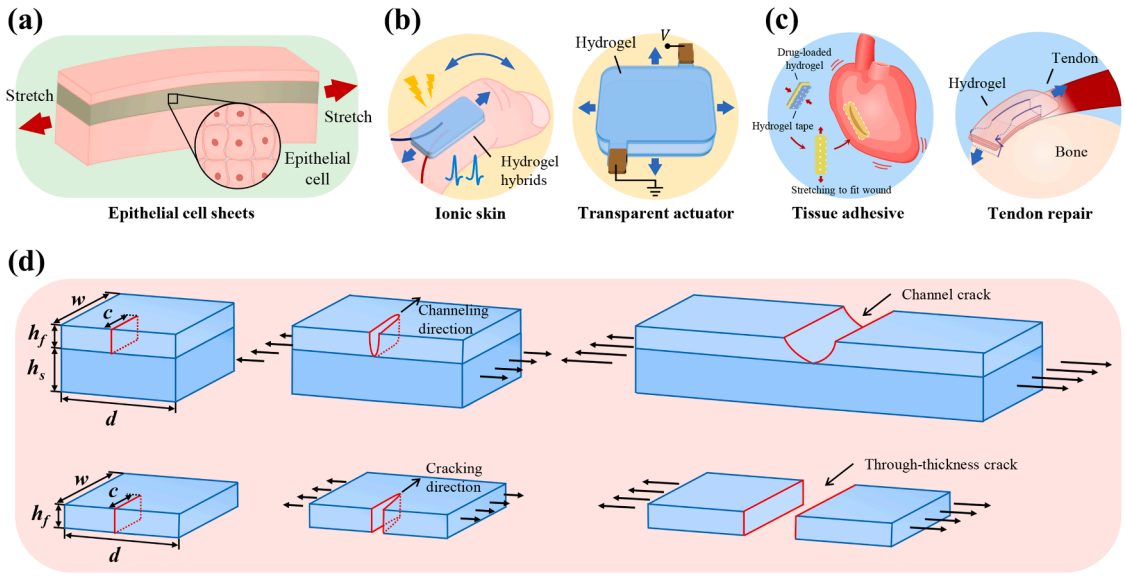

Fig. 1. Soft layered materials and their fracture patterns. (a) Natural soft layered materials such as epithelial cell sheets. Examples of synthetic soft layered materials include (b) hydrogel ionic skin and actuator for engineered functional devices, and (c) tissue adhesive and tendon repair for biomedical applications. (d) Schematic diagrams showing the distinct fracture modes of homogeneous monolayer soft materials and heterogeneous layered soft materials. Although not shown in the figure, in soft layered materials, channel cracking is often accompanied by concomitant interfacial delamination induced by severe stress concentrations at the channel root, the effects of which will also be considered in this study.

in soft layered materials has received relatively less attention and is far from sufficient, where present studies of their fracture behavior mainly focus on the performance of stretchability or the cracking modes [34–49]. Very recently, Men et al. study the cracking modes in layered hyperelastic structures made of relatively brittle films bonded to tougher substrates, and establish the critical conditions for different cracking modes as well as build the phase diagram [50]. In that work, the channel cracking in the surface layer is proved to be the prevailing fracture mode of soft layered materials, which is often accompanied by the interfacial delamination induced by the stress concentration near the channel root and then co-evolves. Meanwhile, Cai et al. put forth a novel approach to enhance the fracture resistance of hydrogels by introducing layered structures that effectively regulate the energy release rate [51], and this study represents one of the initial efforts in specifically investigating the fracture behavior of heterogeneous layered hydrogels distinct from homogeneous hydrogels, in which the experimentally observed phenomenon of interfacial delamination near the root of channel crack is also documented. However, in the above study the attention is mainly focused on the impact of forming layered structures on soft materials' fracture resistance, where the whole process of co-evolution of channel cracking and interfacial delamination has not been further investigated, and there is still a need for additional research to delve into soft layered materials' unique fracture feature.

In this work, we explore, both experimentally and theoretically, the fracture behavior of heterogeneous soft layered materials. According to classical fracture mechanics, it is well known that homogeneous materials suffer from size-dependent and flaw-sensitive fracture behavior [52–55]: their stretch at break λ_{cr}, at which the material fractures, reduces markedly as the flaw size and overall structural dimensions increase, which is undesirable since flaws can hardly be avoided during fabrication and usage and the structural dimensions have to be sufficiently large for many applications. In sharp contrast, we find that heterogeneous soft layered materials exhibit anomalous size-independent and flaw-insensitive fracture behaviors, where the stretch at break is independent of flaw size and overall structure dimensions, overcoming the inherent limitations of the stretchability of homogeneous soft materials (i.e., flaw sensitivity and size dependence), which is ideal for practical applications in mechanically demanding environments. Hence, based on the above, the distinction and novelty of the present study relative to existing researches on failure mechanics in heterogeneous layered materials and our previous work [51] can be concluded as follows. From the experimental standpoint, the experimental findings and evidence in this study, pertaining to the anomalous size-independent and flaw-insensitive fracture behaviors of soft layered materials, have not been previously addressed in any prior study, including the previous paper of ours [51]. In that work, only qualitative and loose speculations are proposed about the unique fracture behaviors of the substrate-supported hydrogel films based on the theoretical formulas without any solid quantitative computation or experimental evidence. From the theoretical standpoint, previous studies concerning the fracture feature in systems involving stiff films on soft substrates are all based on small deformation theory, where the materials are linear elastic, and their results are inadequate to unveil and explain the size-independent fracture behaviors in soft film/soft substrate systems considering the nonlinear elasticity. While in studies focused on soft-film soft-substrate systems, a comprehensive theoretical framework is absent for analyzing the co-evolving channel cracking and interfacial delamination, posing significant challenges in investigating the whole process from the lateral interfacial delamination in the wake of the channel crack to the steady-state crack channeling with accompanying delamination. The rest of the paper is organized as follows. Employing PAAm-PAA bilayer hydrogels as the representative soft layered material system, Section 2 experimentally reveals the unique fracture behavior of heterogeneous soft layered materials, by comparing the fracture processes between bilayer hydrogels and their homogeneous monolayer counterparts. Section 3 develops a theoretical framework for analyzing the co-evolving channel cracking and interfacial delamination in systems consisting of soft films on soft substrates, which is then applied to investigate the fracture of bilayer hydrogel systems. The results of theoretical analysis and corresponding numerical simulations agree well with the experimentally observed anomalous flaw-insensitive and size-independent fracture behavior of bilayer hydrogels, explaining the mechanism underpinning the unusual fracture behavior. Concluding remarks are provided in Section 4.

2. Experimental section

Aiming for revealing the unique fracture behavior of heterogeneous soft layered materials, in this section we employ PAAm-PAA bilayer hydrogels as the representative soft layered material system, and experimentally compare the fracture processes between them and their homogeneous monolayer counterparts.

2.1. Material selection

To experimentally study the anomalous fracture behavior of soft layered materials, we first need to design and fabricate a representative soft layered material – which is determined as a hydrogel bilayer consisting of two distinct hydrogel layers, including a hydrogel film and a stretchable hydrogel substrate, considering that the heterogeneity renders channel cracking in the surface layer the prevailing fracture mode of soft layered materials [34,50] (Fig. 1d). For this purpose, polyacrylamide (PAAm) hydrogels and poly-(acrylic acid) (PAA) hydrogels are chosen to fabricate the bilayer structure as they can adhere well and fast, based on a well-established fact in chemistry: the carboxyl groups on PAA and the amide groups on PAAm can form hydrogen bonds [56] that confer instant and relatively tough adhesion between them. Note here that subject to interfacial toughness constraints of common soft materials (such as the PAA and PAAm hydrogels selected in this paper), the interfacial delamination at the channel root is unavoidable for the severe stress concentrations [51], whose effect will also be taken into consideration in the following sections.

2.2. Sample preparation

We purchased hydrogel monomers including acrylic acid (AA, A800293) and acrylamide (AAm, A800656) from Macklin. N, N'-methylenebis (acrylamide) (MBAA, M7279) and α-ketoglutaric acid (75890) were purchased from Sigma-Aldrich. All chemicals are used directly upon receipt without further purification.

To synthesize the PAA hydrogel, 6.255 g AA, 0.0088 g N, N'-methylenebis (acrylamide) (MBAA, 0.14 wt% of AA), and 0.0125 g α-ketoglutaric acid (0.2 wt% of AA) are added into 30 ml of deionized water sequentially, where the AA, MBAA, and α-ketoglutaric acid serve as the monomer, cross-linker, and photo-initiator, respectively, to obtain the precursor solution for PAA hydrogel. Then the precursor solution is injected into an acrylic mold – an acrylic spacer sandwiched by two pieces of acrylic plates. Note that to prevent the hydrogel from adhering to the acrylic mold, we treat the mold with commercial glass water repellent before the injection of the precursor solution. After 2 h curing under 365 nm UV radiation (8 W), a thin rectangular PAA hydrogel sheet is obtained with the required dimensions.

To synthesize the PAAm hydrogel, 6.809 g AAm is added to 50 ml of deionized water first. Then we add 0.0041 g MBAA (0.06 wt% of AAm) and 0.0136 g α-ketoglutaric acid (0.2 wt% of AAm) into the aqueous solution as the cross-linker and the photo-initiator, respectively. Next, we treat the acrylic mold with commercial glass water repellent and inject the precursor solution into the mold, which is then subjected to 365 nm UV radiation (8 W) for 1 h for curing. The mold shapes the synthesized PAAm hydrogel into a rectangular sheet with the same dimensions as the PAA hydrogel sheet.

To fabricate the bilayer PAAm-PAA hydrogel structures, we first remove the as-synthesized PAA hydrogels and PAAm hydrogels from the mold with tweezers and then immediately put them into clean sample bags separately to avoid contamination. After 20 min, the PAAm and PAA hydrogels are taken out from the sample bag and a precut is introduced in the PAA hydrogel with a razor blade. Next, the two hydrogel sheets are immediately brought together under ambient conditions without applying any contact pressure. The contact time is set to 30 s before testing, and then instant and tough adhesion is formed between the two hydrogel layers, as expected, owing to the noncovalent hydrogen bonds formed between the carboxyl groups on PAA and the amide groups on PAAm.

2.3. Mechanical testing

To reveal the unique fracture behavior of soft layered materials, we first experimentally investigate homogeneous monolayer poly-(acrylic acid) hydrogels (PAA hydrogels) with flaws (i.e., pre-cuts) as control studies. The tests are performed using the mechanical testing machine SAS CMT-6103 with a 50 N load cell. Prior to testing, each end of the prepared hydrogel sample is sandwiched by two acrylic plates, and then the entire structure is clamped to the clamping fixtures of the testing machine. In the tests, the samples are stretched in the direction perpendicular to the pre-crack with a loading rate of 30 mm/min. Fig. 2a–c show the fracture process of three homogeneous PAA hydrogels under uniaxial tension and record their stretch at break λ_{cr} at which the pre-cut begins to propagate. Note that the value of $\lambda_{cr} - 1$ gives the fracture strain of a material according to continuum mechanics, and thus measures the stretchability of materials. In Fig. 2a, a monolayer PAA hydrogel with dimensions of 8 mm (width w) × 6.8 mm (height d, the distance between the two grips) × 1.5 mm (thickness) is presented as a baseline case – where the width w and height d define the overall dimensions of the hydrogel. Its flaw size is given by $c/w = 0.2$ – where c denotes the length of the pre-cut. We acquire images of the homogeneous hydrogel at different levels of applied deformation (Fig. 2a). The pre-cut in the PAA hydrogel remains stationary when the applied stretch λ is small and turns into a running crack at $\lambda_{cr} = 3.4$, fracturing the hydrogel. For a monolayer PAA hydrogel of the same overall dimensions but a longer flaw size $c/w = 0.5$ (Fig. 2b), the stretch at break λ_{cr}drops to 3 relative to the baseline case. The results indicate that the fracture behavior of homogeneous hydrogel is flaw-sensitive, i.e., the stretch at break reduces with increasing flaw size, which poses a significant challenge to the reliability of materials because the introduction of flaws is almost inevitable during fabrication and use of materials [57]. In addition, as shown in Fig. 2c, compared to the baseline case, a PAA hydrogel with the same normalized flaw size $c/w = 0.2$ but larger overall dimensions [20 mm (width) × 17 mm (height)] possesses a markedly lower stretch at break $\lambda_{cr} = 2.4$. That is, the fracture behavior of homogeneous hydrogels undesirably depends on the overall hydrogel size: larger homogeneous hydrogels – sometimes required by specific applications – exhibit lower stretchability.

We next study the fracture behavior of soft layered materials with the identical experimental setup, by employing PAAm-PAA bilayer hydrogels as a representative soft layered material system as previously noted, which consist of pre-notched PAA hydrogel films adhered to PAAm hydrogel (i.e., polyacrylamide hydrogels) substrates. Both PAA and PAAm layers are 1.5 mm thick for PAAm-PAA layered hydrogels throughout this paper. As mentioned above, one salient feature of the stretched PAAm-PAA bilayer hydrogels is the interfacial delamination near the crack (Fig. 2e), whose influence on the fracture behavior of soft layered materials should not be ignored and will be investigated in the next section. By comparing the fracture processes of bilayer hydrogels to their homogeneous monolayer counterparts, we reveal the anomalous fracture behavior of layered soft materials with three unique advantages: (i) Flaw insensitivity. The comparison of Fig. 2d and e shows that as the normalized flaw size c/w increases from 0.2 to 0.5, the stretches at break of PAAm-PAA bilayer hydrogels remain unchanged at $\lambda_{cr} = 4.5$, independent of the flaw size, which is in sharp contrast to the flaw-sensitive fracture behavior of homogenous hydrogels. (ii) Overall size independence. By contrasting Fig. 2d and f, we find that, when the in-plane structural dimensions increase by a factor of 2.5 – from 8 mm × 6.8 mm to 20 mm × 17 mm – the stretches at break λ_{cr} of the bilayer hydrogels remain at $\lambda_{cr} = 4.5$, not affected by the overall dimensions of hydrogels, defeating the conflict between size and stretchability for homogeneous hydrogels. (iii) Stretchability enhancement. Comparing results of each row of Fig. 2 (e.g., Fig. 2a versus Fig. 2d) shows that, for

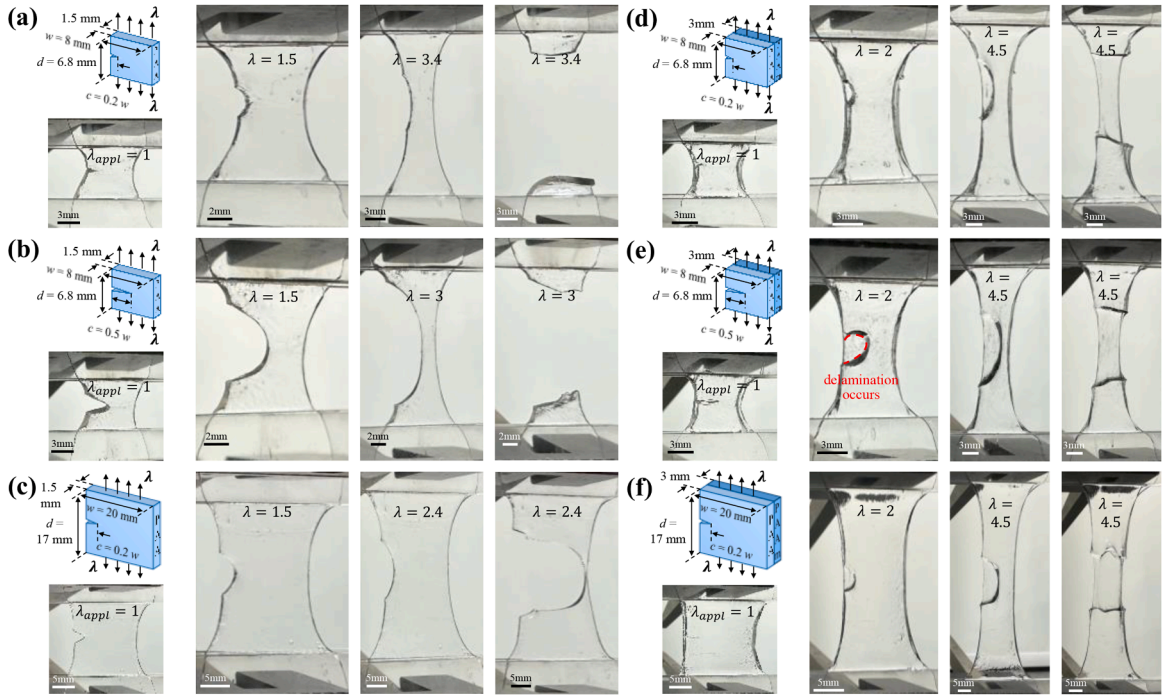

Fig. 2. Fracture tests of homogeneous monolayer PAA hydrogels and heterogeneous bilayer PAAm-PAA hydrogels. (a–c) Photographs of homogeneous monolayer PAA hydrogels with different overall sizes and flaw lengths subject to various stretches. These three pre-notched monolayer PAA hydrogels rupture at stretches of 3.4, 3, and 2.4, respectively, showing size-dependent and flaw-sensitive fracture resistance. (d–f) Photographs of heterogeneous bilayer PAAm-PAA hydrogel structures subject to different stretches. Despite the various flaw lengths and overall dimensions of the three samples, the pre-cracks in the PAA layer remain stationary until the stretch reaches 4.5 for all the samples, indicating anomalous size-independent and flaw-insensitive fracture behavior of heterogeneous bilayer hydrogels. The dimensions of all samples are given in the corresponding schematics. In (e), the red dotted lines emphasize the phenomenon of interfacial delamination observed.

the same in-plane overall dimensions and normalized flaw size, heterogeneous bilayer hydrogels exhibit higher stretches at break than homogeneous hydrogels. The underlying mechanism is that the PAAm layer can effectively restrain the crack opening displacement of the pre-cracked PAA layer and reduce the energy release rate for crack propagation, thereby increasing the stretchability of bilayer hydrogels.

To further experimentally verify the anomalous fracture behavior of soft layered materials observed in Fig. 2, we perform uniaxial tensile tests on a series of homogeneous PAA hydrogels and bilayer PAAm-PAA hydrogels with various normalized flaw sizes and overall dimensions, and measure their stretchability. The experimental setup remains unchanged, and for each experimental data point illustrated in Figs. 3 and 4, we test at least 5 samples to calculate the mean and standard deviation. Fig. 3 depicts the stretch at break λ_{cr} as a function of the normalized flaw size c/w, with overall dimensions of the PAA and PAAm layers being set to 20 mm (width) × 17 mm (height) × 1.5 mm (thickness). The normalized flaw sizes are taken to be $c/w = 0.1, 0.2, 0.5, 0.7$, respectively. In Fig. 4, stretches at break of monolayer and bilayer hydrogels of different in-plane dimensions – which are 8 mm × 6.8 mm, 14 mm × 11.9 mm, 20 mm × 17 mm, and 26 mm × 22.1 mm – are plotted, where the normalized flaw size c/w is fixed to 0.5. The data in Figs. 3 and 4 further confirm the anomalous fracture behavior of bilayer hydrogels compared to monolayer hydrogels: The stretches at break of homogeneous hydrogels show a continuous drop with increasing normalized flaw size c/w (Fig. 3) or overall in-plane dimensions (Fig. 4), indicating that homogeneous hydrogels containing longer flaws or having larger overall dimensions are more prone to fracture, which is in good agreement with classical fracture mechanics [53]. In striking contrast, the stretches at break of bilayer hydrogels are independent of the normalized flaw size and in-plane overall dimensions (Figs. 3 and 4), overcoming the inherent limitations of the fracture behavior of monolayer hydrogels – flaw sensitivity and size dependence. Furthermore, thanks to the unique flaw-insensitive and size-independent fracture

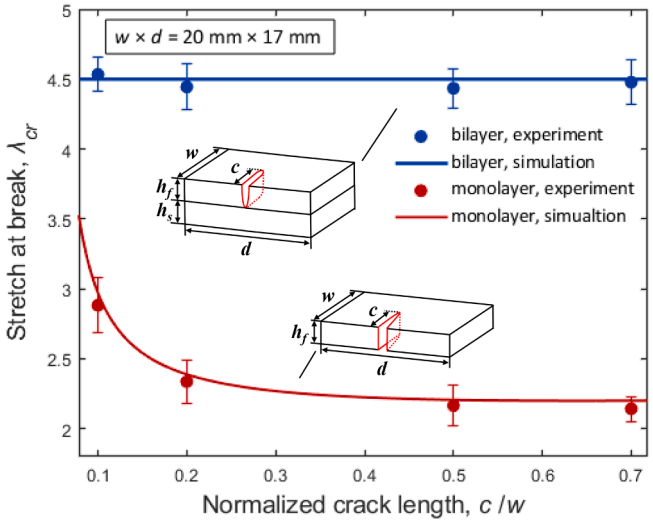

Fig. 3. The experimentally measured and numerically simulated stretches at break plotted as a function of the normalized crack length c/w. The in-plane dimensions of the PAA and PAAm samples are fixed to 20 mm × 17 mm. The monolayer PAA hydrogel sheet exhibits stretch at break λ_{cr} depending on normalized crack length c/w. In stark contrast, the stretch at break λ_{cr} of heterogeneous bilayer PAAm-PAA hydrogel structure well exceeds that of homogeneous monolayer hydrogel and, more intriguingly, is independent of the normalized crack length c/w. The simulation results (solid lines) for monolayer and bilayer hydrogels – which will be discussed in detail in Sections 3.1 and 3.2, respectively – are well in line with the experimental measurements (dots).

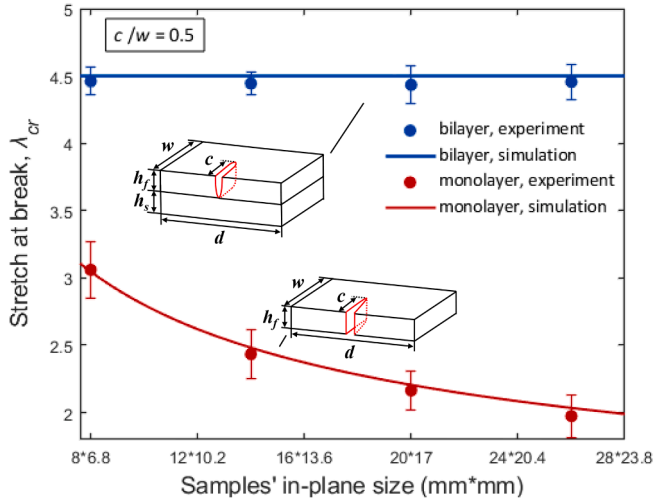

Fig. 4. The experimentally measured and numerically simulated stretches at break plotted as a function of the in-plane dimensions of the sample. The normalized crack length is fixed at $c/w = 0.5$. The stretch at break λ_{cr} of homogeneous monolayer PAA hydrogel sheet depends on the in-plane dimensions of the sample. In contrast, the stretch at break λ_{cr} of heterogeneous bilayer PAAm-PAA hydrogels is independent of the in-plane dimensions of the hydrogel and shows an evident increase compared with homogeneous monolayer hydrogel sheet. See Sections 3.1 and 3.2 for discussions of the simulation results (solid lines) that agree well with the experimental measurements (dots).

behavior of bilayer hydrogels, there exists a huge enhancement in the stretches at break of bilayer hydrogels compared to their monolayer counterparts, especially when the flaw is long and the hydrogel size is large (Figs. 3 and 4).

3. Theoretical analysis and numerical simulations

In the previous section, we have experimentally demonstrated the anomalous flaw-insensitive and size-independent fracture behavior of bilayer hydrogels. To understand the above experimental results, in this section, we carry out theoretical analysis and numerical simulations of both monolayer and bilayer hydrogels, respectively, under uniaxial stretch.

3.1. Fracture behavior of homogeneous monolayer hydrogels

Consider a pre-notched monolayer hydrogel film subject to uniaxial stretch λ (Fig. 5a). The material is taken to be hyperelastic and incompressible with a shear modulus μ_f. Note that the crack opening displacement in monolayer hydrogels is uniform across the film thickness h_f (Fig. 1d), such that the deformation of the hydrogel can be obtained by solving a plane-stress boundary-value problem, where the relevant length scales include the flaw length c, the film width w, and the film height d. To this end, dimensional analysis dictates that the energy release rate G_m associated with the pre-crack (i.e., the flaw) advancing a unit distance takes the form that

$$G_m = g\left(\frac{c}{w}, \frac{w}{d}, \lambda\right)\mu_f c. \tag{1}$$

Herein, the subscript m refers to monolayer hydrogels. The dimensionless function g depends on three dimensionless parameters: the normalized flaw size c/w, the aspect ratio of the hydrogel w/d, and the applied stretch λ. Notably, for stretched hydrogels with a given combination of c, w, d, and λ, the energy release rate G_m can be calculated as the J-integral [58] using finite element package ABAQUS. Then the value of the function $g\left(\frac{c}{w}, \frac{w}{d}, \lambda\right)$ can be computed accordingly based on Eq. (1).

The flaw of length c in monolayer hydrogels starts to advance when the energy release rate reaches the fracture toughness of the hydrogel, i.e., $G_m = \Gamma_f$. Plugging the fracture criterion into Eq. (1) gives the dimensionless equation of critical condition for steady-state crack propagation in monolayer hydrogels that

$$g\left(\frac{c}{w}, \frac{w}{d}, \lambda_{cr}\right) = \frac{\Gamma_f}{\mu_f c}. \tag{2}$$

By further defining a new dimensionless function $p\left(\frac{c}{w}, \frac{w}{d}, \lambda\right) = \left(\frac{c}{w}\right) g\left(\frac{c}{w}, \frac{w}{d}, \lambda\right)$, we can rewrite Eq. (2) as

$$p\left(\frac{c}{w}, \frac{w}{d}, \lambda_{cr}\right) = \frac{\Gamma_f}{\mu_f w}. \tag{3}$$

Eqs. (2) and (3) indicate that the stretch at break λ_{cr} of monolayer hydrogels depends on flaw length c as well as in-plane overall dimensions w (and d), indicating the flaw sensitivity and size dependence of the fracture behavior of monolayer hydrogels.

Next, to verify the experimental results of monolayer hydrogels shown in Figs. 3 and 4, stretch at break λ_{cr} for steady-state crack propagation in monolayer hydrogels is numerically determined based on the above-mentioned analysis. To this end, we calculate the energy release

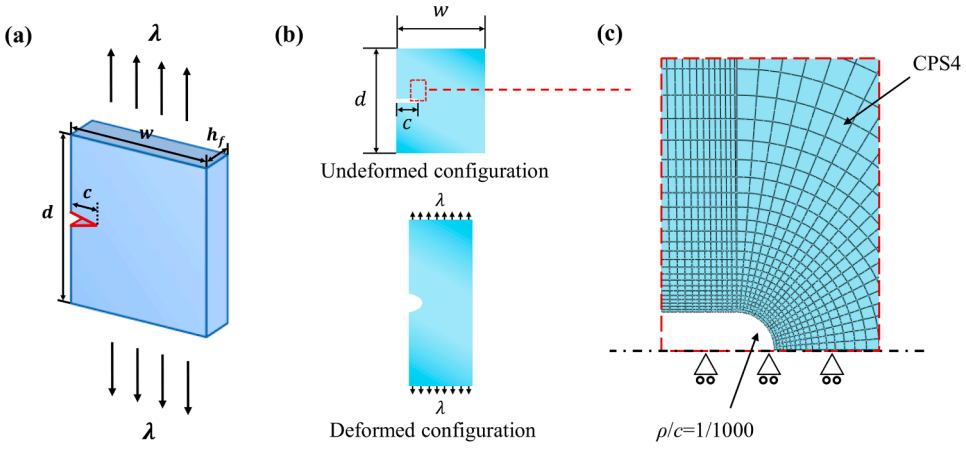

Fig. 5. Computational model for calculating the energy release rate for crack propagation in homogeneous monolayer hydrogels. (a) Schematics of a hydrogel sheet with a pre-crack of length c. (b) The characteristic dimensions of the pre-notched hydrogel sheet. In the undeformed state, the width and height of the sheet are w and d, respectively. The length of the crack is c. In the deformed state, the hydrogel sheet is pulled to a length of λd. (c) The blunted crack tip modeled with a finite radius ρ. The hydrogel sheet is densely meshed with CPS4 elements in ABAQUS.

rate G_m as the J-integral [58] using the finite element code ABAQUS. Then, values of the dimensionless function $g\left(\frac{c}{w}, \frac{c}{d}, \lambda\right)$ can be computed according to Eq. (1), and stretch at break λ_{cr} can subsequently be obtained by solving Eq. (2). In the simulations to calculate G_m, we model a pre-notched hydrogel sheet of width w, height d, and crack length c, as shown in Fig. 5b. Here, these geometry dimensions of the sheet are set to be identical to those of the monolayer PAA samples used in the aforementioned experiments. The hydrogel sheet is under a vertical stretch λ. Incompressible neo-Hookean model with shear modulus $\mu_f = 3$ kPa is adopted for the hydrogel according to the mechanical test on PAA hydrogels (Appendix A). Considering the symmetry of the geometry, only the top half of the hydrogel sheet is modeled, where the symmetric boundary condition is set along the symmetry plane and the stretch λ is exerted on the upper edge of the model. A blunt crack tip, with a small radius $\rho = c/1000$ in the undeformed configuration, is modeled to avoid singularity at the crack tip. The model is meshed with CPS4 elements, with dense meshes in the region near the crack tip (Fig. 5c).

Given the above numerical solving of dimensionless function $g\left(\frac{c}{w}, \frac{c}{d}, \lambda\right)$, once the fracture toughness Γ_f of the hydrogel film is given, stretch at break λ_{cr} of the monolayer hydrogel sheet can be determined using Eq. (2). To obtain the theoretical results (i.e., red solid lines) in Figs. 3 and 4, $w = 20$ mm and $d = 17$ mm are taken for Fig. 3, while $\frac{c}{w} = 0.5$ and $\frac{w}{d} = \frac{20}{17}$ are employed for Fig. 4, both consistent with the hydrogel dimensions used in the experiments. As can be seen from Figs. 3 to 4, when setting the hydrogel sheet's fracture toughness $\Gamma_f = 69.9$ J/m^2 according to the pure-shear test (Appendix B), the theoretical predictions match the experimental results (i.e., red dots in Figs. 3 and 4) very well, which shows that stretches at break decrease with increasing flaw length and overall sample size, confirming the flaw-sensitive and size-dependent fracture behavior of homogeneous hydrogels.

3.2. Fracture behavior of heterogeneous bilayer hydrogels

3.2.1. A theoretical framework of co-evolving channel cracking and interfacial delamination

We next consider a bilayer hydrogel under uniaxial stretch λ, which

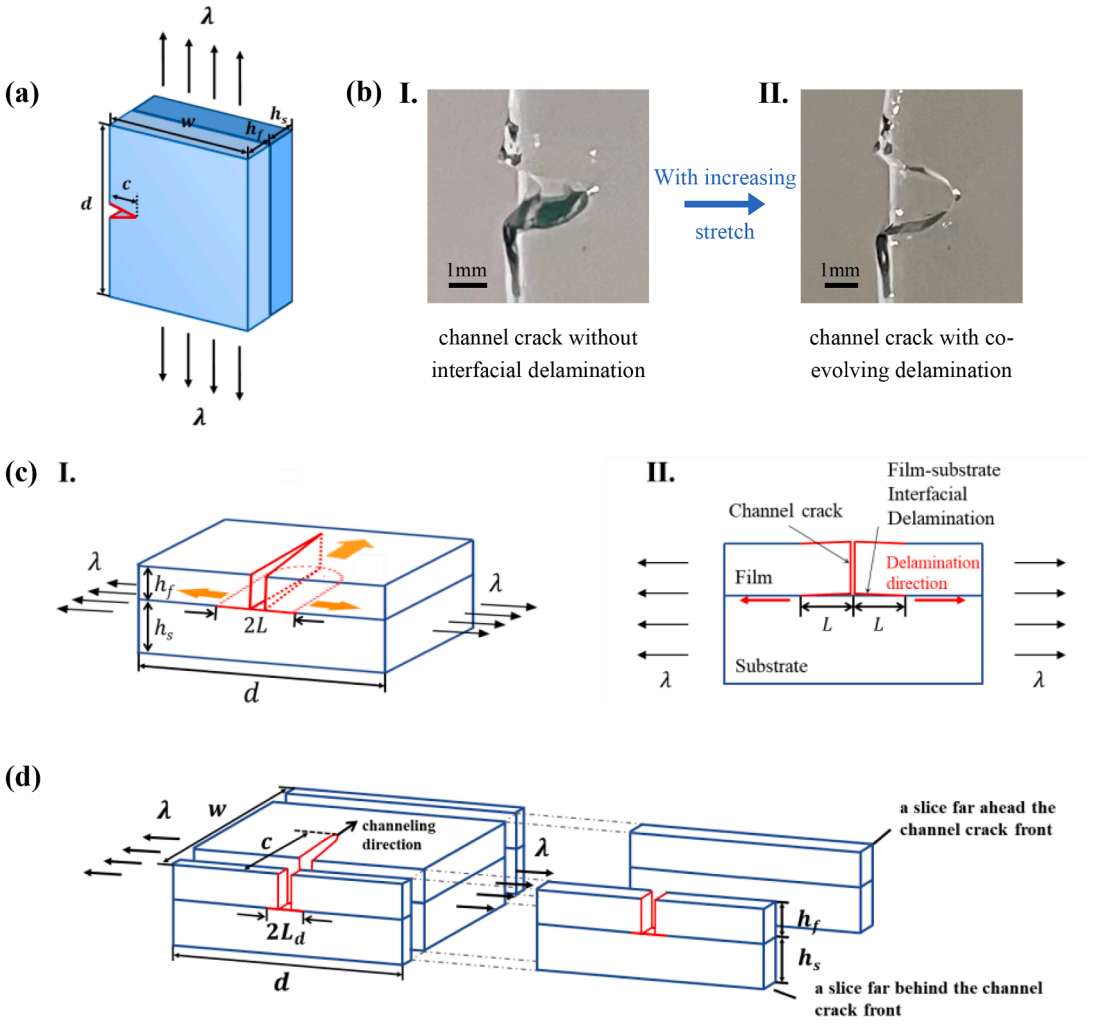

Fig. 6. Simulations of the fracture process of heterogeneous bilayer hydrogels. (a) Schematics of a bilayer hydrogel consisting of a pre-notched hydrogel film adhered to a hydrogel substrate. (b) The experimentally observed interfacial delamination in heterogeneous bilayer PAAm-PAA hydrogels. Photographs showing the crack morphology (I) without and (II) with interfacial delamination, respectively. With increasing stretch, interfacial delamination occurs in the proximity of the crack root, then co-evolves with the channel crack. (c) The computational model for the determination of the interfacial delamination length L_d. (I) Schematics of the propagation of interfacial delamination in the wake of the channel crack. (II) Finite element model for calculating the energy release rate for lateral interfacial delamination in the direction of tension. (d) The computational model for calculating the energy release rate of the channel crack and the accompanying interfacial delamination (i.e., the $\perp$-shaped crack) in heterogeneous bilayer hydrogels. The elastic energy released by the channel crack and the accompanying interfacial delamination advancing a unit distance equals to the elastic energy stored in a slice of material of unit thickness far ahead of the crack front minus the elastic energy stored in a slice of material of unit thickness far behind the crack front.

consists of a pre-notched PAA hydrogel layer (i.e., the film) adhered to a PAAm hydrogel layer (i.e., the substrate) (Fig. 6a). Considering that a salient feature of stretched bilayer hydrogels observed in the experiments is the interfacial delamination near the root of channel crack (Fig. 6b), whose effect on the crack pattern and the driving force of cracking has been demonstrated to be not negligible [51,59], a theoretical framework is developed for analyzing the co-evolving channel cracking and interfacial delamination in systems consisting of soft films on soft substrates to study the fracture behavior of bilayer hydrogels and then explain the experimental results.

The co-evolution of film cracking and interfacial delamination is a prevalent phenomenon observed in substrate-film bilayer systems subjected to large deformation [60–62], owing to the mutual facilitation between channel cracking and interfacial delamination. For one thing, the severe stress concentration at the interface in close proximity to the channel root stimulates interfacial delamination. For another, the partial detachment of the film from the substrate engenders an augmented driving force, propelling the propagation of channel cracks. Fig. 6c illustrates this co-evolution of channel crack and interfacial delamination in bilayer hydrogels under uniaxial tension. When subjected to sufficiently large tension, the stress concentration near the channel root becomes pronounced, leading to the initiation of interfacial delamination. As to be shown later, during the propagation of interfacial delamination, its driving force drops as it advances along the direction of tension. As a consequence, when the driving force decreases to a level lower than the interfacial toughness, the propagation of interfacial delamination in the tensile direction ceases, ending up with a delamination length L_d in the undeformed configuration [63]. On the other hand, the vertical channel crack and the accompanying horizontal interfacial delamination of length L_d together form a ⊥-shaped crack, and continue to propagate in the direction normal to the applied tension (Fig. 6c). This process is defined as the steady-state co-evolution of channel crack and interfacial delamination.

3.2.1.1. Interfacial delamination along tensile direction in the wake of the channel crack. In this section, we first consider lateral interfacial delamination emanating from the root of the channel crack (Fig. 6c I). Note here that for a long, straight channel crack, the bilayer hydrogel can be regarded as deforming under the plane strain conditions far behind the channel front. Focus on the energy release rate for propagation of interfacial delamination in the tensile direction G_d, dimensional considerations indicate that it takes a form that

$$G_d = q\left(\frac{h_s}{h_f}, \frac{\mu_s}{\mu_f}, \frac{L}{h_f}, \lambda\right)\mu_f h_f \tag{4}$$

Then the normalized energy release rate for delamination far behind the channel root can be defined as: $\frac{G_d}{\mu_f h_f} = q\left(\frac{h_s}{h_f}, \frac{\mu_s}{\mu_f}, \frac{L}{h_f}, \lambda\right)$. Herein, the dimensionless function q depends on four dimensionless parameters: the thickness ratio h_s/h_f and shear modulus ratio μ_s/μ_f between the substrate and film, the normalized delamination length L/h_f, and the stretch λ.

To evaluate the normalized energy release rate $G_d/\mu_f h_f$ for any given combination of h_s/h_f, μ_s/μ_f, L/h_f, and λ, we simulate a slice of material of unit thickness far behind the crack front (Fig. 6c II), and the driving force for interfacial delamination along the direction of tension G_d can be computed as the energy release rate at the delaminating front using the J-integral function provided by ABAQUS. In the simulations, the length of the film–substrate interfacial delamination is set to be L on each side of the channel root. Regarding the overall dimensions, the height and the width of the slices are identical to those of the bilayer PAAm-PAA samples used in the experiments, i.e., $w = 20$ mm and $d = 17$ mm. The slices are meshed with the CPE4RH element (i.e., the four-node bilinear hybrid plane strain quadrilateral element with reduced integration). To guarantee the precision of the computation, the region in the proximity of the delamination front in the slice far behind the crack front is densely meshed. Regarding boundary conditions, a stretch λ parallel to the hydrogel layers is applied to the lateral sides of the slices. The incompressible neo-Hookean model is adopted for both the hydrogel film and substrate. In the simulations, as suggested by Eq. (4), we vary the thickness ratio h_s/h_f and the shear modulus ratio μ_s/μ_f, respectively, to investigate its effect on the energy release rate for interfacial delamination.

Fig. 7a plots the calculated normalized energy release rate at the delamination front in the direction of tension (i.e., the normalized driving force for lateral interfacial delamination) $G_d/\mu_f h_f$ as a function of the applied stretch λ for various thickness ratios h_s/h_f, with shear modulus ratio fixed at $\mu_s/\mu_f = 0.2$. In contrast, in plotting Fig. 7b, we set the thickness ratio $h_s/h_f = 1$ but vary the shear modulus ratio μ_s/μ_f. The normalized delamination length $L/h_f = 1$ is employed for Fig. 7a and b. As evident in the figures, the normalized energy release rate rises nonlinearly with increasing applied stretches and is more significantly affected by the shear modulus ratio compared with the thickness ratio. Then, in Fig. 7c and d, $G_d/\mu_f h_f$ is plotted as a function of normalized delamination length L/h_f for various thickness ratios h_s/h_f and shear modulus ratios μ_s/μ_f, respectively. The shear modulus ratio μ_s/μ_f is set to 0.2 for Fig. 7c, and the thickness ratio $h_s/h_f = 1$ is set for Fig. 7d. For both figures the applied stretch λ is fixed to 5. As illustrated in Fig. 7c and d, the normalized energy release rate decreases with increasing delamination length and changes little when the thickness ratio varies. When the delamination length is small, the normalized energy release rate decreases as the shear modulus ratio μ_s/μ_f increases. While for large delamination, an opposite trend is seen as the normalized energy release rate increases when the shear modulus ratio increases. The trends can be understood as follows: For small interfacial delamination, the crack opening displacement in the top hydrogel film can be constrained by the bottom hydrogel substrate; a stiff substrate can more effectively restrain the opening of interfacial cracks. Therefore, the stiffer the substrate, the lower the normalized energy release rate $G_d/\mu_f h_f$ for interfacial delamination. And when the delamination length is large, the constraint of the substrate become weaker. In such conditions, under a given stretch, the elastic energy stored in the substrate increases as the shear modulus of the substrate increases, resulting in more elastic energy released during the advancement of interfacial delamination.

According to fracture mechanics theory, the initiation and propagation of interfacial delamination are contingent upon the comparison between the driving force, G_d, and the interfacial toughness, Γ_i. As revealed in the figure, at the channel root, it is possible for delamination to initiate when the film-substrate interfacial toughness is modest, as the driving force for interfacial delamination is markedly large for small delamination length due to the pronounced stress concentration around the channel root. However, it can be observed that the driving force progressively decreases as the delamination propagates along the interface between the film and substrate in the tensile direction. Once the driving force decreases to the value equal to the interfacial toughness (i.e., $G_d = \Gamma_i$), the propagation of delamination comes to a halt with the final delamination length being L_d. Substituting Eq. (4) into the above equation, the steady-state delamination length L_d can be obtained by solving the following dimensionless equation,

$$q\left(\frac{h_s}{h_f}, \frac{\mu_s}{\mu_f}, \frac{L_d}{h_f}, \lambda\right) = \frac{\Gamma_i}{\mu_f h_f} \tag{5}$$

The geometric significance of Eq. (5) is also illustrated in Fig. 7: once the normalized adhesion energy $\Gamma_i/\mu_f h_f$ (represented by the horizontal dashed lines in Fig. 7) is given, one can determine L_d by finding the intersection of the dashed line and the calculated energy release rate curve in Fig. 7c and d. In the following sections, we will numerically obtain this steady-state delamination length L_d for subsequent analysis of the steady-state channel cracking.

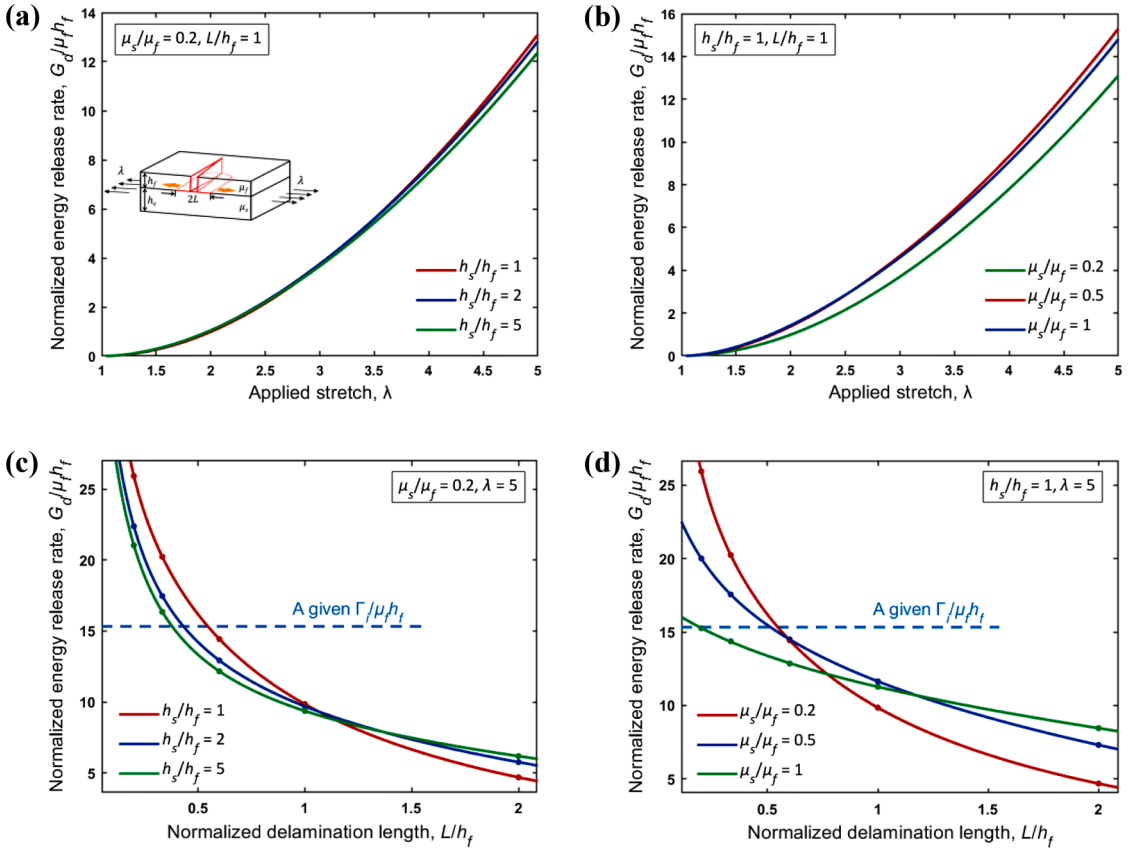

Fig. 7. The normalized energy release rate for interfacial delamination along tensile direction in bilayer hydrogels. (a) $G_d/\mu_f h_f$ plotted as a function of the applied stretch λ for various normalized substrate thickness h_s/h_f. The shear modulus ratio μ_s/μ_f is fixed at 0.2. Inset: schematics of the bilayer hydrogel with lateral interfacial delamination. (b) $G_d/\mu_f h_f$ as a function of the applied stretch λ for various normalized substrate shear modulus μ_s/μ_f. The fixed thickness ratio $h_s/h_f = 1$ is used. The normalized delamination length $L/h_f = 1$ is employed for (a) and (b). (c) $G_d/\mu_f h_f$ plotted as a function of normalized delamination length L/h_f for various normalized substrate thickness h_s/h_f, where the fixed shear modulus ratio $\mu_s/\mu_f = 0.2$. (d) $G_d/\mu_f h_f$ as a function of normalized delamination length L/h_f for various normalized substrate shear modulus μ_s/μ_f and the thickness ratio h_s/h_f is fixed to 1. For both (c) and (d) the applied stretch λ is fixed to 5.

3.2.1.2. The steady-state channel cracking with concomitant interfacial delamination. Then, we consider the steady-state ⊥-shaped crack propagation in the direction perpendicular to the applied tension, where far behind the channel crack front the delamination reaches a constant length of L_d as analyzed above. Both layers are taken to be incompressible hyperelastic materials. It should be noted that for bilayer hydrogel systems, propagation of channel crack will reach a steady state upon the crack length c reaching a few times the film thickness h_f [64,65]. After that, the crack opening displacement profile becomes uniform along the channel cracking direction and remains unchanged as the crack advances, which is no longer affected by the crack length c and the in-plane overall dimensions w and d. Taking the above considerations into account, through dimensional analysis, we can identify the elastic energy U released as the channel crack and the accompanying interfacial delamination advancing a unit distance as follows,

$$U = f\left(\frac{h_s}{h_f}, \frac{\mu_s}{\mu_f}, \frac{L_d}{h_f}, \lambda\right)\mu_f h_f^2. \tag{6}$$

Herein, the dimensionless function f depends on four dimensionless parameters including the thickness ratio h_s/h_f and shear modulus ratio μ_s/μ_f between the substrate and film, the normalized delamination length L_d/h_f, and the stretch λ.

Then the energy release rate for the ⊥-shaped crack to advance in the direction perpendicular to the applied stretch can be written in a form similar to Eq. (4) as

$$G_b = U/h_f = f\left(\frac{h_s}{h_f}, \frac{\mu_s}{\mu_f}, \frac{L_d}{h_f}, \lambda\right)\mu_f h_f. \tag{7}$$

The subscript b refers to bilayer hydrogels. As mentioned above, by finding the intersection of the straight line representing normalized adhesion energy and the numerically calculated energy release rate curve for lateral interfacial delamination, L_d can be determined for any given combination of h_s/h_f, μ_s/μ_f, λ, and $\Gamma_i/\mu_f h_f$. Following this, the released elastic energy U can be computed by the elastic energy stored in a slice of material of unit thickness far ahead of the crack front minus the elastic energy stored in a slice of material of unit thickness far behind the crack front [64] (Fig. 6d), where the elastic energies of the two slices are obtained by numerically solving two plane-strain boundary-value problems, and the energy release rate G_b can be evaluated by U/h_f after U is calculated.

3.2.2. The application of the theoretical framework: the determination of the stretch at break for bilayer hydrogels

Aiming at comparing theoretical predictions with experimental results shown in Figs. 3 and 4, we subsequently employ the theoretical framework developed to determine the stretch at break of bilayer hydrogel structures – at which the channel crack in the hydrogel film and the concomitant film-substrate interfacial delamination start propagating steadily perpendicular to the tensile direction. The criterion for steady-state ⊥-shaped crack propagation is given by $G_b = \Gamma_f + 2\Gamma_i L_d/h_f$ [35], where Γ_f is the fracture toughness of the pre-notched layer (PAA hydrogel in this work) and Γ_i is the toughness of the bilayer interface.

Substituting the fracture criterion into Eq. (7) yields the critical condition in a dimensionless form as follows,

$$f\left(\frac{h_s}{h_f}, \frac{\mu_s}{\mu_f}, \frac{L_d}{h_f}, \lambda_{cr}\right) = \frac{\Gamma_f}{\mu_f h_f} + \frac{2\Gamma_i L_d}{\mu_f h_f^2}. \tag{8}$$

Notably, in contrast to Eqs. (2) and (3) for homogeneous hydrogels, Eq. (8) does not contain crack length c and in-plane overall dimensions w and d. Therefore, the stretch at break λ_{cr} – i.e., the solution of Eq. (8) for bilayer hydrogels is irrelevant to the flaw length and the hydrogel's in-plane dimensions.

To numerically evaluate this stretch at break λ_{cr}, we model a slice of material of unit thickness far ahead of the channel crack front and a slice of material of unit thickness far behind the crack front, and obtain the energy release rate G_b through computing the elastic energy difference between the two slices as previously noted. The simulations are conducted with the commercial finite element code ABAQUS. Also, we compute the driving force for interfacial delamination in the direction of tension again, to determine the steady-state delamination length L_d, as the energy release rate at the delamination front in the slice far behind the crack front.

In the simulation, the overall dimensions, namely the height and the width of the slices as well as the thicknesses of the substrate and film, are also set to be identical to those of the PAAm-PAA experimental samples. That is, $w = 20$ mm and $d = 17$ mm are adopted for obtaining the theoretical results in Fig. 3, $\frac{w}{d} = \frac{20}{17}$ is employed for Fig. 4, $h_f = h_s = 1.5$ mm are used for both figures. The material parameters are set as $\mu_f = 3$ kPa, $\mu_s = 2.4$ kPa and $\Gamma_f = 69.9$ J/m^2 according to the mechanical tests (Appendix A and B), and the interfacial toughness Γ_i of the PAAm-PAA interface is taken to be 63 J/m^2 according to the literature [56]. In the simulations, based on the criterion for steady-state co-evolving channel cracking and delamination, we vary the applied stretch λ to determine the stretch at break λ_{cr} for steady-state crack propagation. The rest of the simulation settings remain the same as in previous simulation for calculating the energy release rate for interfacial delamination G_d.

Fig. 8a plots the calculated energy release rate G_d for interfacial delamination along the tensile direction as a function of normalized delamination length L/h_f for various applied stretches λ. It can be observed from the figure that, as noted before, delamination may start to form at the channel root, and the driving force drops as it advances in the tensile direction. When the driving force falls to a level in line with the adhesion energy, i.e., $G_d = \Gamma_i$, propagation of the delamination will ultimately stop, where the final delamination length is L_d. Hence, from the interfacial toughness Γ_i of the PAAm-PAA interface valuing 63 J/m^2 (represented by the horizontal dashed line in Fig. 8a) evaluated by the literature [56], we can determine the normalized steady-state delamination length L_d/h_f in the undeformed configuration under any given applied stretch λ – by identifying the intersection point between the dashed line and the corresponding energy release rate curve calculated in Fig. 8a.

Meanwhile in Fig. 8b, the energy release rate for steady-state $\perp$-shaped crack propagation G_b for various applied stretches λ is plotted as a function of the normalized steady-state delamination length L_d/h_f, and it can be noticed in the figure that G_b increases significantly as the steady-state delamination length increases. This can be explained by the vast quantities of elastic energy released from the newly formed delaminated region of the hydrogel film in propagation of the channel cracking and the concomitant interfacial delamination because of losing substrate constraint. For instance, G_b increases almost fourfold when $L_d/h_f = 2$ compared with the case $L_d/h_f = 0.1$ when $\lambda = 4.5$. In contrast, without interfacial delamination, only a confined region in the hydrogel film along the channel crack surface is relaxed and thus the elastic

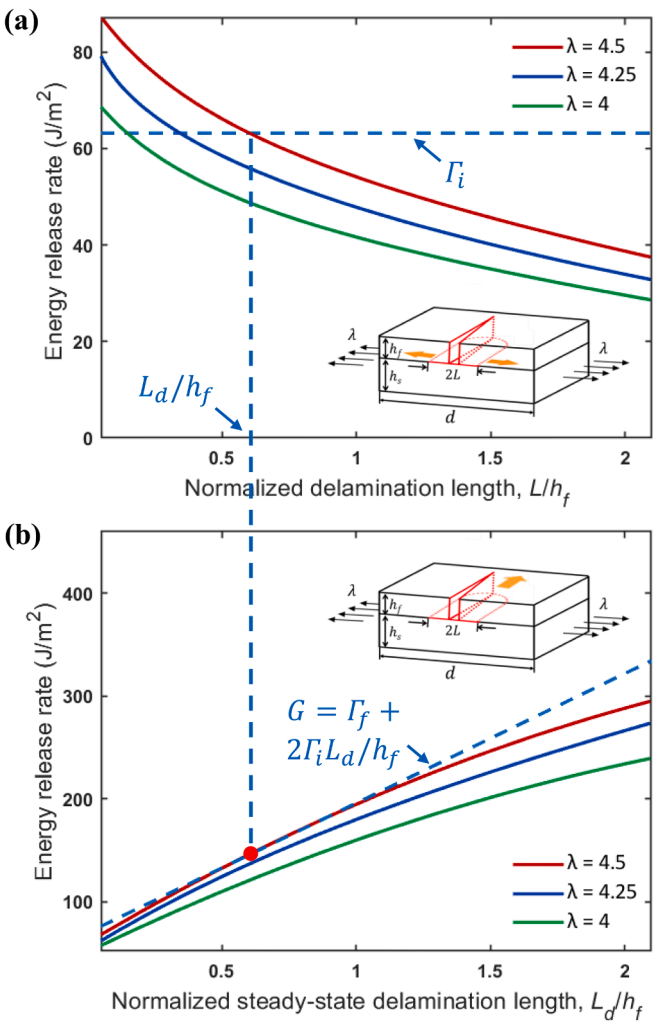

Fig. 8. Simulation results of the co-evolving channel cracking and interfacial delamination. (a) Energy release rate for interfacial delamination along tensile direction as a function of normalized delamination length L/h_f. Inset: schematics of the interfacial delamination along tensile direction. (b) Energy release rate for channel cracking and concomitant interfacial delamination perpendicular to tensile direction as a function of normalized steady-state delamination length L_d/h_f. Inset: schematics of the steady-state channel cracking and interfacial delamination perpendicular to tensile direction. Dash lines: based on the interfacial toughness Γ_i of the PAAm-PAA interface evaluated by the literature, the normalized steady-state delamination length L_d/h_f under any given applied stretch λ can be determined from (a), from which the stretch at break λ_{cr} for steady-state crack propagation can be further determined in (b) with the criterion for steady-state co-evolving channel cracking and interfacial delamination $G_b = \Gamma_f + 2\Gamma_i L_d/h_f$.

energy released will be modest. As previously discussed, the steady-state delamination length L_d for any given applied stretch λ can be determined in Fig. 8a, by finding the intersection of the horizontal dashed line symbolizing the interfacial toughness and the energy release rate curve. Then from the obtained normalized steady-state delamination length L_d/h_f, which is represented by the vertical dashed line in Fig. 8, we can evaluate the energy release rate G_b for steady-state crack propagation under that stretch by identifying the intersection point of the vertical dashed line and the corresponding energy release rate curve in Fig. 8b.

To this end, one can determine whether a given stretch is the stretch

at break λ_{cr} for steady-state crack propagation based on whether the energy release rate for it satisfying the criterion for steady-state ⊥-shaped crack propagation (represented by the dashed straight line in Fig. 8b). For instance, as illustrated in Fig. 8a, when setting $\lambda = 4$ the intersection between the horizontal dashed line and the green energy release rate curve determines the normalized steady-state delamination length $L_d/h_f = 0.152$. Correspondingly in Fig. 8b, from the obtained L_d/h_f and the calculated green energy release rate curve, the energy release rate G_b for steady-state crack propagation can be evaluated at 69.9, noticeably lower than the value on the dashed straight line corresponds to $L_d/h_f = 0.15$. Apparently, this discrepancy indicates that $\lambda = 4$ is not the critical stretch at which the propagation of steady-state ⊥-shaped crack – comprising both channel crack and concomitant interfacial delamination – occurs. At an increased applied stretch of $\lambda = 4.25$, following the same method, it can be found that the obtained G_b still remains below the corresponding value on the dashed straight line in Fig. 8b. Eventually, by increasing the applied stretch to 4.5, G_b satisfies the criterion for steady-state channel cracking and delamination, for it matching the vertical coordinate value on the dashed straight line in Fig. 8b, and the stretch at break for steady-state crack propagation $\lambda_{cr} = 4.5$ has been determined through this procedure.

As is conveyed by Figs. 3 and 4, following the procedure for determining the stretch at break λ_{cr} described above, the theoretical results – which are represented by the solid blue lines in the figure – are in good agreement with the experimental measurements (i.e., blue dots), further confirming the anomalous fracture behavior of soft layered materials, exemplified by their advantages of flaw insensitivity and size independence.

4. Conclusions and remarks

In this work, we experimentally and theoretically uncover the anomalous fracture behavior of soft layered materials and the underlying physics by investigating bilayer hydrogels – a representative layered soft material. It is revealed that the stretch at break of soft layered materials is independent of the flaw size and the overall dimensions of the soft material, and thus they exhibit significantly enhanced stretch at break than homogeneous soft materials. This is a highly desirable feature absent for common homogeneous hydrogels: the larger the hydrogel dimensions or the longer the flaw size, the lower the stretch at break, leading to reduced mechanical reliability. In comparison, soft layered materials containing long flaws or having large sizes can maintain high stretchability because of their anomalous size-independent and flaw-insensitive fracture behavior.

The findings presented in this study universally hold for a broad range of soft materials such as hydrogels, elastomers, and biological tissues, unveiling the mechanical mechanism underpinning the prevalence of soft layered materials in natural selection and engineering design. One example is the epithelium of diverse organs that possess layered structures, whose superior stretchability comes from its independence of the flaw size and overall dimensions, so that it can function robustly under repeated significant levels of stretch during adult life [66], which is a potent stimulus for growth, differentiation, remodeling and gene expression [22,67,68]. Results in this work offer a universal and feasible-to-implement approach to designing tough soft materials with size-independent fracture behaviors for a broad spectrum of applications [69], which advance existing research on the fracture behaviors and toughening methods of soft materials [70].

CRediT authorship contribution statement

Yijie Cai: Formal analysis, Methodology, Investigation, Software, Data curation, Writing – original draft. **Shaoxing Qu:** Resources, Writing – review & editing, Supervision. **Zheng Jia:** Conceptualization, Methodology, Resources, Writing – review & editing, Supervision, Funding acquisition.

Declaration of competing interest

The authors declare that they have no known competing financial interests or personal relationships that could have appeared to influence the work reported in this paper.

Acknowledgments

This work is supported by the National Key Technologies Research and Development Program (Grant No. 2022YFC3203900), Natural Science Foundation of Zhejiang Province (Grant No. LR22A020005), the National Natural Science Foundation of China (Grant No. 12321002 and 12072314), and the 111 Project (Grant No. B21034).

Appendix A

To evaluate the shear moduli of PAA and PAAm hydrogels used in this work, we measure their uniaxial stress-stretch curves using the mechanical testing machine SAS CMT-6103 with a loading rate of 30 mm/min. Then the experimental data[1] is fitted to the incompressible neo-Hookean model using the curve-fitting module of the finite element code ABAQUS. Fig. A1 shows that proper fit can be obtained under moderate stretches, yielding a shear modulus of 3 kPa for the PAA hydrogel and 2.4 kPa for the PAAm hydrogel.

[1] These experimental data are also used in a previous publication of the authors (Cai et al. [51]) due to the similar material selection.

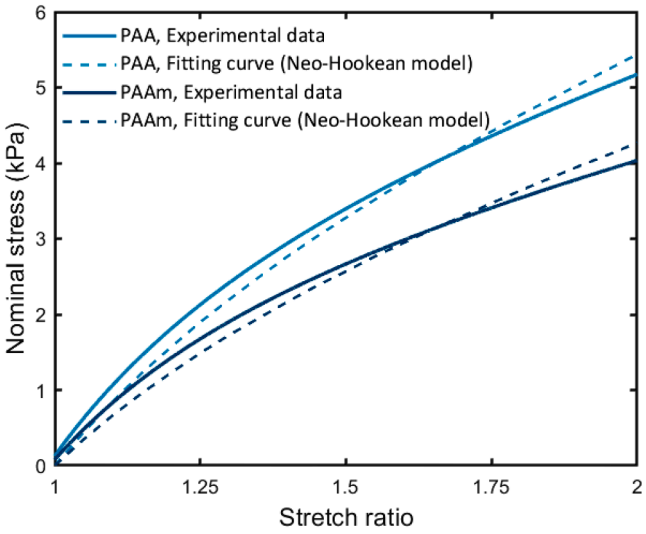

Fig. A1. Stress–stretch curves of PAA and PAAm hydrogels under uniaxial tension. The shear moduli of PAA and PAAm hydrogels are obtained by fitting the incompressible neo-Hookean model (dashed curves) to the experimental stress–stretch curves (solid curves).

Appendix B

To evaluate the fracture toughness Γ_f of the PAA hydrogel film, we conduct pure-shear tests on PAA hydrogels. The dimensions of the PAA samples being tested are 70 mm (width W) × 17 mm (gauge height between grips H) × 1.5 mm (thickness), and the length of the pre-crack is $0.4W$. In the test, the notched PAA sample is stretched to λ_c at which the crack propagates, with the stress-stretch curves recorded as the dark blue lines in Fig. B1. Then, the same stretch λ_c is applied on the unnotched hydrogel sheet and the corresponding stress-stretch curves are recorded (the cyan lines in Fig. B1). The tests are conducted with the mechanical testing machine SAS CMT-6103 and the loading rate is 30 mm/min. Based on the raw data in Fig. B1,[2] the fracture toughness of the hydrogel can be calculated as $\Gamma = H\int_1^{\lambda_c} s\,d\lambda$, where H is the height of the PAA sample and s is the measured nominal stress. The experimentally measured fracture toughness of the three PAA samples is 61.6 J/m^2, 73.2 J/m^2, and 74.9 J/m^2, respectively, where the average is 69.9 J/m^2.

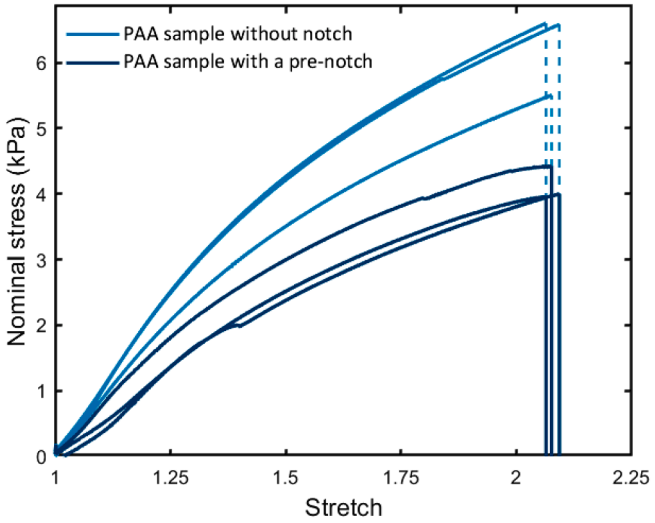

Fig. B1. The nominal stress-stretch curves of PAA hydrogels in pure-shear test for measuring the fracture toughness.

References

[1] Seliktar D. Designing cell-compatible hydrogels for biomedical applications. Science 2012;336:1124–8.

[2] Hoffman AS. Hydrogels for biomedical applications. Adv Drug Deliv Rev 2002;54:3–12.

[3] Zhang YS, Khademhosseini A. Advances in engineering hydrogels. Science 2017;356:eaaf3627.

[2] These experimental data are also used in a previous publication of the authors (Cai et al., 2023) due to the similar material selection.

[4] Norioka C, Inamoto Y, Hajime C, Kawamura A, Miyata T. A universal method to easily design tough and stretchable hydrogels. NPG Asia Mater 2021;13:34.
[5] Wathoni N, Motoyama K, Higashi T, Okajima M, Kaneko T, Arima H. Physically crosslinked-sacran hydrogel films for wound dressing application. Int J Biol Macromol 2016;89:465–70.
[6] Liang Y, He J, Guo B. Functional hydrogels as wound dressing to enhance wound healing. ACS Nano 2021;15:12687–722.
[7] Jeong JW, McCall JG, Shin G, Zhang Y, Al-Hasani R, Kim M, Li S, Sim JY, Jang KI, Shi Y, Hong DY, Liu Y, Schmitz GP, Xia L, He Z, Gamble P, Ray WZ, Huang Y, Bruchas MR, Rogers JA. Wireless optofluidic systems for programmable *in vivo* pharmacology and optogenetics. Cell 2015;162:662–74.
[8] Buwalda SJ, Vermonden T, Hennink WE. Hydrogels for therapeutic delivery: current developments and future directions. Biomacromolecules 2017;18:316–30.
[9] Qazi TH, Burdick JA. Granular hydrogels for endogenous tissue repair. Biomater Biosyst 2021;1:100008.
[10] Ju Y, Hu Y, Yang P, Xie X, Fang B. Extracellular vesicle-loaded hydrogels for tissue repair and regeneration. Mater Today Bio 2023;18:100522.
[11] Han L, Lu X, Wang M, Gan D, Deng W, Wang K, Fang L, Liu K, Chan CW, Tang Y, Weng LT, Yuan H. A mussel-inspired conductive, self-adhesive, and self-healable tough hydrogel as cell stimulators and implantable bioelectronics. Small 2017;13:1601916.
[12] Keplinger C, Sun JY, Foo CC, Rothemund P, Whitesides GM, Suo Z. Stretchable, transparent, ionic conductors. Science 2013;341:984–7.
[13] Haghiashtiani G, Habtour E, Park SH, Gardea F, McAlpine MC. 3D printed electrically-driven soft actuators. Extreme Mech Lett 2018;21:1–8.
[14] Yao L, Yan H, He Y, Zhao N, Wang X, Li C, Sun L, He Y, Liu Y, Zhang J. Actuation performances of catkin fibers reinforced thiol-acrylate main-chain liquid crystalline elastomer. Int J Smart Nano Mater 2022;13:668–90.
[15] Li T, Li G, Liang Y, Cheng T, Dai J, Yang X, Liu B, Zeng Z, Huang Z, Luo Y, Xie T, Yang W. Fast-moving soft electronic fish. Sci Adv 2017;3:e1602045.
[16] Sarwar MS, Dobashi Y, Preston C, Wyss JKM, Mirabbasi S, Madden JDW. Bend, stretch, and touch: locating a finger on an actively deformed transparent sensor array. Sci Adv 2017;3:e1602200.
[17] Larson C, Peele B, Li S, Robinson S, Totaro M, Beccai L, Mazzolai B, Shepherd R. Highly stretchable electroluminescent skin for optical signaling and tactile sensing. Science 2016;351:1071–4.
[18] Wei J, Li L, Li R, Liu Q, Yan Z, Chen T. Dual-imaging-mode smart hydrogel information platform for illumination-independent covert decryption and read. Int J Smart Nano Mater 2022;13:612–25.
[19] Lee Y, Song WJ, Sun JY. Hydrogel soft robotics. Mater Today Phys 2020;15:100258.
[20] Morin SA, Shepherd RF, Kwok SW, Stokes AA, Nemiroski A, Whitesides GM. Camouflage and display for soft machines. Science 2012;337:828–32.
[21] Li X, Yuan L, Liu R, He H, Hao J, Lu Y, Wang Y, Liang G, Yuan G, Guo Z. Engineering textile electrode and bacterial cellulose nanofiber reinforced hydrogel electrolyte to enable high-performance flexible all-solid-state supercapacitors. Adv Energy Mater 2021;11:2003010.
[22] Casares L, Vincent R, Zalvidea D, Campillo N, Navajas D, Arroyo M, Trepat X. Hydraulic fracture during epithelial stretching. Nat Mater 2015;14:343–51.
[23] Lei Z, Wu P. A supramolecular biomimetic skin combining a wide spectrum of mechanical properties and multiple sensory capabilities. Nat Commun 2018;9:1134.
[24] Pu X, Liu M, Chen X, Sun J, Du C, Zhang Y, Zhai J, Hu W, Wang ZL. Ultrastretchable, transparent triboelectric nanogenerator as electronic skin for biomechanical energy harvesting and tactile sensing. Sci Adv 2017;3:e1700015.
[25] Ha KH, Huh H, Li Z, Lu N. Soft capacitive pressure sensors: trends, challenges, and perspectives. ACS Nano 2022;16:3442–8.
[26] Li Z, He X, Cheng J, Li H, Zhang YF, Shi X, Yu K, Yang HY, Ge Q. Hydrogel-elastomer-based stretchable strain sensor fabricated by a simple projection lithography method. Int J Smart Nano Mater 2021;12:256–68.
[27] Jager EWH, Inganäs O, Lundström I. Microrobots for micrometer-size objects in aqueous media: potential tools for single-cell manipulation. Science 2000;288:2335–8.
[28] Feinberg AW, Feigel A, Shevkoplyas SS, Sheehy S, Whitesides GM, Parker KK. Muscular thin films for building actuators and powering devices. Science 2007;317:1366–70.
[29] Nam S, Mooney D. Polymeric tissue adhesives. Chem Rev 2021;121:11336–84.
[30] Yuk H, Varela CE, Nabzdyk CS, Mao X, Padera RF, Roche ET, Zhao X. Dry double-sided tape for adhesion of wet tissues and devices. Nature 2019;575:169–74.
[31] Liu X, Wu M, Wang M, Hu Q, Liu J, Duan Y, Liu B. Direct synthesis of photosensitizable bacterial cellulose as engineered living material for skin wound repair. Adv Mater 2022;34:2109010.
[32] Wang Z, Lee WJ, Koh BTH, Hong M, Wang W, Lim PN, Feng J, Park LS, Kim M, Thian ES. Functional regeneration of tendons using scaffolds with physical anisotropy engineered via microarchitectural manipulation. Sci Adv 2018;4:eaat4537.
[33] Lin S, Liu J, Liu X, Zhao X. Muscle-like fatigue-resistant hydrogels by mechanical training. Proc Natl Acad Sci 2019;116:10244–9.
[34] Cordero N, Yoon J, Suo Z. Channel cracks in a hermetic coating consisting of organic and inorganic layers. Appl Phys Lett 2007;90:111910.
[35] Jia Z, Tucker MB, Li T. Failure mechanics of organic–inorganic multilayer permeation barriers in flexible electronics. Compos Sci Technol 2011;71:365–72.
[36] Li T, Huang ZY, Xi ZC, Lacour SP, Wagner S, Suo Z. Delocalizing strain in a thin metal film on a polymer substrate. Mech Mater 2005;37:261–73.
[37] Lacour SP, Chan D, Wagner S, Li T, Suo Z. Mechanisms of reversible stretchability of thin metal films on elastomeric substrates. Appl Phys Lett 2006;88:204103.
[38] Lu N, Suo Z, Vlassak JJ. The effect of film thickness on the failure strain of polymer-supported metal films. Acta Mater 2010;58:1679–87.
[39] Shao X, Cai Y, Yin S, Li T, Jia Z. Mechanics of interfacial delamination in deep-sea soft robots under hydrostatic pressure. J Appl Mech 2023;90:021009.
[40] An L, Wu X, Wang K, Li R, Li Z, Li G. Crack modes and toughening strategies of bioinspired 3D printed double-helicoidal architectures. Int J Mech Sci 2023;253:108388.
[41] Yekani Fard M, Pensky A. Stochastic multiscale multimode interlaminar fracture toughness of buckypaper nanocomposites. Int J Mech Sci 2023;237:107798.
[42] Li Z, Lin YC, Zhang L, Zheng J, Zhao J, Wang R, Jiang Z. In-situ investigation on tensile properties of a novel Ti/Al composite sheet. Int J Mech Sci 2022;231:107592.
[43] Bosco E, Suiker ASJ, Fleck NA. Crack channelling mechanisms in brittle coating systems under moisture or temperature gradients. Int J Fract 2020;225:1–30.
[44] Askarinejad S, Rahbar N. Mechanics of bioinspired lamellar structured ceramic/polymer composites: experiments and models. Int J Plast 2018;107:122–49.
[45] Ben Bettaieb M, Abed-Meraim F. Investigation of localized necking in substrate-supported metal layers: comparison of bifurcation and imperfection analyses. Int J Plast 2015;65:168–90.
[46] Chen FL, He X, Prieto-Muñoz PA, Yin HM. Opening-mode fractures of a brittle coating bonded to an elasto-plastic substrate. Int J Plast 2015;67:171–91.
[47] Jia Z, Li T. Necking limit of substrate-supported metal layers under biaxial in-plane loading. Int J Plast 2013;51:65–79.
[48] Wu H, Fan G, Huang M, Geng L, Cui X, Xie H. Deformation behavior of brittle/ductile multilayered composites under interface constraint effect. Int J Plast 2017;89:96–109.
[49] Zhou X, Chen C. Strengthening and toughening mechanisms of amorphous/amorphous nanolaminates. Int J Plast 2016;80:75–85.
[50] Men L, Yu Y, Hou Z, Li X, Wang Z. Cracking modes in layered hyperelastic structures. J Mech Phys Solids 2023;174:105254.
[51] Cai Y, Ma J, Shen Z, Shao X, Jia Z, Qu S. Enhancing the fracture resistance of hydrogels by regulating the energy release rate via bilayer designs: theory and experiments. J Mech Phys Solids 2023;170:105125.
[52] Chen C, Wang Z, Suo Z. Flaw sensitivity of highly stretchable materials. Extreme Mech Lett 2017;10:50–7.
[53] Pharr M, Sun JY, Suo Z. Rupture of a highly stretchable acrylic dielectric elastomer. J Appl Phys 2012;111:104114.
[54] Akhtar S, Bhowmick AK, De PP, De SK. Tensile rupture of short fibre filled thermoplastic elastomer. J Mater Sci 1986;21:4179–84.
[55] Hamed GR. Effect of crosslink density on the critical flaw size of a simple elastomer. Rubber Chem Technol 1983;56:244–51.
[56] Wang Y, Jia K, Xiang C, Yang J, Yao X, Suo Z. Instant, tough, noncovalent adhesion. ACS Appl Mater Interfaces 2019;11:40749–57.
[57] Zeng L, Liu F, Yu Q, Jin C, Yang J, Suo Z, Tang J. Flaw-insensitive fatigue resistance of chemically fixed collagenous soft tissues. Sci Adv 2023;9:eade7375.
[58] Rice JR. A path independent integral and the approximate analysis of strain concentration by notches and cracks. J Appl Mech 1968;35:379–86.
[59] Liu M, Yu S, He L, Ni Y. Recent progress on crack pattern formation in thin films. Soft Matter 2022;18:5906–27.
[60] Li T, Suo Z. Ductility of thin metal films on polymer substrates modulated by interfacial adhesion. Int J Solids Struct 2007;44:1696–705.
[61] Lu N, Wang X, Suo Z, Vlassak J. Failure by simultaneous grain growth, strain localization, and interface debonding in metal films on polymer substrates. J Mater Res 2009;24:379–85.
[62] Lu N, Wang X, Suo Z, Vlassak J. Metal films on polymer substrates stretched beyond 50%. Appl Phys Lett 2007;91:221909.
[63] Mei H, Pang Y, Huang R. Influence of interfacial delamination on channel cracking of elastic thin films. Int J Fract 2007;148:331–42.
[64] Hutchinson JW, Suo Z. Mixed mode cracking in layered materials. J.W. Hutchinson, T.Y. Wu. Advances in applied mechanics. Elsevier; 1991. p. 63–191.
[65] Huang R, Prévost JH, Huang ZY, Suo Z. Channel-cracking of thin films with the extended finite element method. Eng Fract Mech 2003;70:2513–26.
[66] Fung YC. Biomechanics: mechanical properties of living tissues. New York: Springer; 2013.
[67] Fink J, Carpi N, Betz T, Bétard A, Chebah M, Azioune A, Bornens M, Sykes C, Fetler L, Cuvelier D, Piel M. External forces control mitotic spindle positioning. Nat Cell Biol 2011;13:771–8.
[68] Miller CJ, Davidson LA. The interplay between cell signalling and mechanics in developmental processes. Nat Rev Genet 2013;14:733–44.
[69] Billiet T, Vandenhaute M, Schelfhout J, Van Vlierberghe S, Dubruel P. A review of trends and limitations in hydrogel-rapid prototyping for tissue engineering. Biomaterials 2012;33:6020–41.
[70] Brodnik NR, Brach S, Long CM, Ravichandran G, Bourdin B, Faber KT, Bhattacharya K. Fracture diodes: directional asymmetry of fracture toughness. Phys Rev Lett 2021;126:025503.